AGU ADVANCING EARTH AND SPACE SCIENCES

Earth and Space Science

RESEARCH ARTICLE
10.1029/2025EA004622

A New Global Climatological Model of the Equatorial Ionospheric Vertical E × B Drift: Integrating Ground-Based Magnetometer, Radar, and Satellite Data Sets

John Bosco Habarulema[1,2,3], Daniel Okoh[4,5], Endawoke Yizengaw[6], Valence Habyarimana[7], Michael Pezzopane[8], Paulo Roberto Fagundes[9], Zama Katamzi-Joseph[1,2,10], Mark B. Moldwin[11], Claudio Cesaroni[8], and Danny Scipion[12]

[1]South African National Space Agency, Hermanus, South Africa, [2]Department of Physics and Electronics, Rhodes University, Makhanda, South Africa, [3]Centre for Space Research, North–West University, Potchefstroom, South Africa, [4]School of Physics and Earth Sciences, The Technical University of Kenya, Nairobi, Kenya, [5]National Space Research and Development Agency, Abuja, Nigeria, [6]Space Science Application Laboratory, The Aerospace Corporation, El Segundo, CA, USA, [7]Department of Physics, Mbarara University of Science and Technology, Mbarara, Uganda, [8]Istituto Nazionale Geofisica e Vulcanologia (INGV), Roma, Italy, [9]Laboratório de Física e Astronomia, Universidade do Vale do Paraíba (UNIVAP), São José Dos Campos, Brazil, [10]School of Agriculture and Science, University of KwaZulu-Natal, Durban, South Africa, [11]Department of Climate and Space Sciences and Engineering, University of Michigan, Ann Arbor, MI, USA, [12]Radio Observatorio de Jicamarca, Instituto Geofísico del Perú, Lima, Perú

Key Points:

- A new global empirical model for the equatorial ionospheric F region drifts is presented
- The proposed model agrees with existing climatology in identifying general features of F region drifts
- Our results improve upon the current climatology model's estimation of vertical **E** × **B** drift by about 23% when compared with ICON's IVM drifts

Correspondence to:

J. B. Habarulema,
jhabarulema@sansa.org.za

Citation:

Habarulema, J. B., Okoh, D., Yizengaw, E., Habyarimana, V., Pezzopane, M., Fagundes, P. R., et al. (2026). A new global climatological model of the equatorial ionospheric vertical E × B drift: Integrating ground-based magnetometer, radar, and satellite data sets. *Earth and Space Science*, *13*, e2025EA004622. https://doi.org/10.1029/2025EA004622

Received 11 JUL 2025
Accepted 24 FEB 2026

Author Contributions:

Conceptualization: John Bosco Habarulema
Data curation: Daniel Okoh, Endawoke Yizengaw, Valence Habyarimana, Michael Pezzopane
Formal analysis: John Bosco Habarulema, Daniel Okoh
Investigation: John Bosco Habarulema
Methodology: John Bosco Habarulema, Daniel Okoh, Endawoke Yizengaw
Resources: John Bosco Habarulema, Daniel Okoh
Software: Daniel Okoh
Validation: John Bosco Habarulema, Daniel Okoh, Michael Pezzopane
Writing – original draft: John Bosco Habarulema
Writing – review & editing: John Bosco Habarulema, Daniel Okoh, Endawoke Yizengaw, Valence Habyarimana,

Abstract We present a new empirical vertical **E** × **B** drift model developed using ground-based magnetometer, radar, and satellite data over equatorial latitude regions. We first implement an algorithm relating magnetometer derived equatorial electrojet (EEJ) and vertical ion plasma drift (equivalent to vertical **E** × **B** drift within magnetic latitudes of ±5° and altitudes of about 400–550 km) from the Communications and Navigation Outage Forecasting System (C/NOFS) satellite at different longitude sectors. The relationship between EEJ and C/NOFS vertical **E** × **B** drift is developed separately at different longitudes over the globe at coincidental times when both data sets are available. These relationships are then used to estimate continuous vertical **E** × **B** drift at each epoch of EEJ observation over the respective longitude sectors during local daytime. The reconstructed vertical **E** × **B** drift data are combined with global C/NOFS vertical **E** × **B** drifts and JULIA data set to develop a global vertical **E** × **B** drift model. Validation using Ion Velocity Meter (IVM) drifts from ICON satellite for January to August 2022 shows that our model improves vertical **E** × **B** drift global modeling by over 20% compared to the current climatology representation.

1. Introduction

Ionospheric vertical **E** × **B** drift studies, especially during geomagnetically disturbed conditions (for example, Huang et al., 2005), continue to generate considerable interest in the scientific community mainly due to the extent of variability in ionospheric electrodynamics at different longitudes. Vertical **E** × **B** drifts play a crucial role on the behavior of the equatorial ionization anomaly regions. Assembling accurate empirical vertical **E** × **B** drift remains a complicated task due to the global data scarcity. To date, the only source of long-term equatorial ionospheric vertical **E** × **B** drift is the incoherent scatter radar (ISR) at Jicamarca (11.8°S, 77.2°W). Satellite missions with drift meter onboard include Dynamic Explorer-B (Coley & Heelis, 1989), Atmospheric Explorer E, AE-E (for example, Scherliess & Fejer, 1999), Republic of China Satellite, ROCSAT (for example, Fejer et al., 2008), Communications and Navigation Outage Forecasting System, C/NOFS (Dubazane & Habarulema, 2018; Stoneback et al., 2011) and Ionospheric Connection Explorer, ICON (Heelis et al., 2022; Hysell et al., 2024). A major drawback of satellite measurements is that the data are not continuous in time over a certain location, although satellite data have better global coverage. The first quiet time global equatorial vertical drift model was presented by Scherliess and Fejer (1999) based on Jicamarca ISR and Ion Drift Meter (IVM) data from the AE-E satellite. In their work, Scherliess and Fejer (1999) detailed the experimental and observational progress in vertical drift studies since 1970s. Since then, there has been improvements and understanding of equatorial electrodynamics. Alken (2009) presented a quiet time equatorial vertical plasma drift using 150 km echoes. The currently recommended model within the International Reference Ionosphere, IRI (Bilitza et al., 2022) is an empirical vertical **E** × **B** drift model based on ROCSAT observations (for example, Fejer et al., 2008). Recently, Shidler and Rodrigues (2020) presented a quiet time ionospheric vertical plasma drift over Jicamarca based on

Michael Pezzopane, Paulo Roberto Fagundes, Zama Katamzi-Joseph, Mark B. Moldwin, Claudio Cesaroni, Danny Scipion

Table 1
Pairs of Magnetometers That Provided Data for Determining EEJ Used in Model Development

Magnetometer site and code	Country	Geographic latitude	Geographic longitude	Magnetic latitude	Available data
Addis Ababa, AAE	Ethiopia	9.0	38.8	0.2	2008–2013
Adigrat, ETHI	**Ethiopia**	14.3	39.5	6	
Abuja, ABJA	Nigeria	8.99	7.38	−1.53	2011–2018
Yaounde, CMRN	**Cameroon**	3.87	11.5	−5.3	
Alta Floresta, ALTA	Brazil	−9.9	−56.1	0.8	2011–2016
Cuiaba, CUIB	**Brazil**	−15.6	−56.1	−5.9	
Belem Station, BELM	Brazil	−1.45	−48.5	−1.05	2015–2018
Petrolina, PETR	**Brazil**	−9.5	−40.5	−6.95	
Conakry, CNKY	Guinea	10.5	−13.7	−0.5	2013–2016
Abidjan, ABAN	**Cote d'Ivoire**	4.6	−6.6	−6.0	
Jicamarca, JICA	Peru	−11.95	−76.87	0.8	2008–2019
Piura, PIUR	**Peru**	−5.2	−80.6	6.8	
Puerto Maldonado, PUER	Peru	−12.6	−69.2	0.0	2009–2018
Leticia, LETI	**Brazil**	−4.2	−69.9	8.2	
Phuket, PUKT	Thailand	7.9	98.4	−0.6	2014–2016
Bangkok, BANG	**Thailand**	14.1	100.6	6.2	

Note. The magnetometer locations displaced off the magnetic equator by 6–9° are indicated in bold.

machine learning. What has been lacking in existing modeling efforts is the continuous representation of longitudinal variability of vertical drifts which is addressed in this current study. We present an innovative approach of combining ground-based magnetometer, C/NOFS satellite, and radar data to develop a global vertical plasma drift model. What is significant is that ground-based magnetometer data allows us to continuously (at least during local daytime) represent different longitude sectors that were earlier not possible to take into account (e.g., African sector) during such modeling efforts.

2. Data Sources and Methodology

2.1. Data Sources

The first three sources of vertical $\mathbf{E} \times \mathbf{B}$ drift data were used in model development while the last data source provided an independent data set for validation.

1. Ground-based magnetometer data: The well known differential magnetometer approach is used to obtain equatorial electrojet (EEJ). This method requires magnetometer locations at the equator and off the equator by 6–9° (for example, Anderson et al., 2004; Yizengaw & Moldwin, 2009; Yizengaw et al., 2011; Yizengaw & Groves, 2018). Magnetometer data are provided by the AMBER (Yizengaw & Moldwin, 2009), SAMBA (Boudouridis & Zesta, 2007) and LISN (Valladares & Chau, 2012) networks. To remove different offset values from each magnetometer data set, nighttime baseline values in H component for each day are determined by averaging H values within 2300–0300 local time and subtracted from the corresponding magnetometer measurements (Yizengaw et al., 2014). Once this is completed, the H component values (with baseline values removed) are directly subtracted to estimate the EEJ. The resulting EEJ data are used to estimate daytime ionospheric vertical $\mathbf{E} \times \mathbf{B}$ drift at all longitudes with magnetometer locations suitable for deriving EEJ. This is done by developing scaling algorithms that transform EEJ into vertical $\mathbf{E} \times \mathbf{B}$ drift based on satellite (C/NOFS) data set. Table 1 shows equatorial magnetometer locations with data available for the estimation of EEJ that was later used in model construction. In the table, for each magnetometer pair, the location that is off the equator by 6–9° is indicated in bold. Details of relating C/NOFS vertical $\mathbf{E} \times \mathbf{B}$ drift and EEJ are given in Section 2.3.

After scaling EEJ (ΔH) to C/NOFS vertical $\mathbf{E} \times \mathbf{B}$ drift, the relationship is used to generate continuous $\mathbf{E} \times \mathbf{B}$ drift over respective magnetometer locations at 1 min resolution.

2. C/NOFS satellite observations: We use the in situ ion vertical drift provided by the Ion Velocity Meter (IVM) instrument onboard C/NOFS satellite as the equivalent of ionospheric vertical $\mathbf{E} \times \mathbf{B}$ drift within the magnetic latitudes of ±5° and altitude range of 400–550 km (for example, Dubazane & Habarulema, 2018; Stoneback et al., 2011). To establish the relationship between EEJ and C/NOFS vertical $\mathbf{E} \times \mathbf{B}$ drift, we use satellite data within ±7.5° longitude of the magnetometer location meridian (for example, Yizengaw et al., 2014; Yizengaw & Groves, 2018) to avoid considerable local time changes in electrodynamics. C/NOFS satellite data from 2008 to 2015 are further averaged at 1 min resolution for the purpose of developing EEJ and C/NOFS vertical $\mathbf{E} \times \mathbf{B}$ drift relationship.
3. ISR data set: Historically, the Jicamarca ISR has been instrumental in revealing vertical and zonal electrodynamic properties of the equatorial ionosphere (for example, Fejer et al., 1979; Scherliess & Fejer, 1999). The Jicamarca ISR provides vertical drifts usually at a 5 min and 15 km time and altitude resolutions, respectively (Kudeki et al., 1999), but is not run continuously due to financial costs and power constraints. However the ISR makes it possible to obtain the 150 km echoes from the Jicamarca Unattended Long-Term studies of the Ionosphere and Atmosphere (JULIA) mode that have been shown to be proxies of the F2 vertical $\mathbf{E} \times \mathbf{B}$ drift during local daytime (for example, Anderson et al., 2002, 2004; Chau & Woodman, 2004). The JULIA data set with temporal resolution of 5 min was first used in validation of magnetometer data derived vertical drifts. Thereafter, JULIA data during 2001–2015 were combined with global C/NOFS and magnetometer derived vertical drifts in the final development of the overall vertical $\mathbf{E} \times \mathbf{B}$ drift model.
4. ICON satellite data: The ICON satellite launched in October 2019 carried an IVM instrument used for determining in situ plasma velocity, ion number density and temperature (Immel et al., 2023). Due to the solar minimum conditions in 2019–2021, a combination of low plasma density and light ion contamination led to inaccurate drift velocity determination especially during morning local times (Immel et al., 2023). Due to this constraint, we have used only 2022 ICON IVM drifts for model validation, which served as a completely independent data set as its data are not incorporated in the empirical model. Validation is done using version 8 revision 2 (v08r002) of the IVM data set that has been corrected "for offsets in ion drifts in the instrument frame." This correction is necessary because the plasma drift measurement can be significantly affected by low O^+ density due to low solar flux levels (for example, Hysell et al., 2024). IVM drift data is selected following recommended quality control flags indicated as $ICON\_L27\_RPA\_Flag$ and $ICON\_L27\_DM\_Flag$ which are assigned values of 1 and 0 representing data to be used with "Caution" and "Good" data set, respectively. We have used the data set corresponding to the data quality flag value of 0 (Good), that is, $ICON\_L27\_RPA\_Flag = ICON\_L27\_DM\_Flag = 0$.

Figure 1 shows the solar activity coverage of the data sets used in model development. JULIA data set is shown at 13 LT for convenience purposes. While the data availability shows an extended coverage with respect to solar activity (represented by F10.7 in black dots), the long duration data set (dating back to 2001) is over one location, Jicamarca. Magnetometer data starts in 2008 and are available during different periods at different longitude sectors as shown in Table 1. Vertical red dashed lines indicate the time period 2022 used for the final model validation.

2.2. Neural Networks

Because of their capabilities in mimicking different functions of various forms and shapes, neural networks have been described as universal approximators in literature (for example, Scarselli & Tsoi, 1998). The challenges and strengths of applying machine learning methods in solving space physics problems have been presented in Camporeale (2019). One of the pioneering works in using neural networks in modeling vertical $\mathbf{E} \times \mathbf{B}$ drift was by Anderson et al. (2004) and in fact established the relationship between magnetometer derived ΔH (proxy of EEJ) and F region drifts. We have used feedforward neural networks to transform a multi-dimensional input space of certain dimension to an output (in this case vertical $\mathbf{E} \times \mathbf{B}$ drift) through a process known as training. Supervised learning has been implemented where the training set consisting of inputs and output are presented to the feedforward network. Because of the randomness associated with neural network initialization, optimization of weights and bias vectors requires a training algorithm. For each training pattern (inputs-target combination), the network output is compared to actual target parameter. Once the entire training data set has been trained, the network weights are adjusted and training process continued until they are optimized. For its robustness

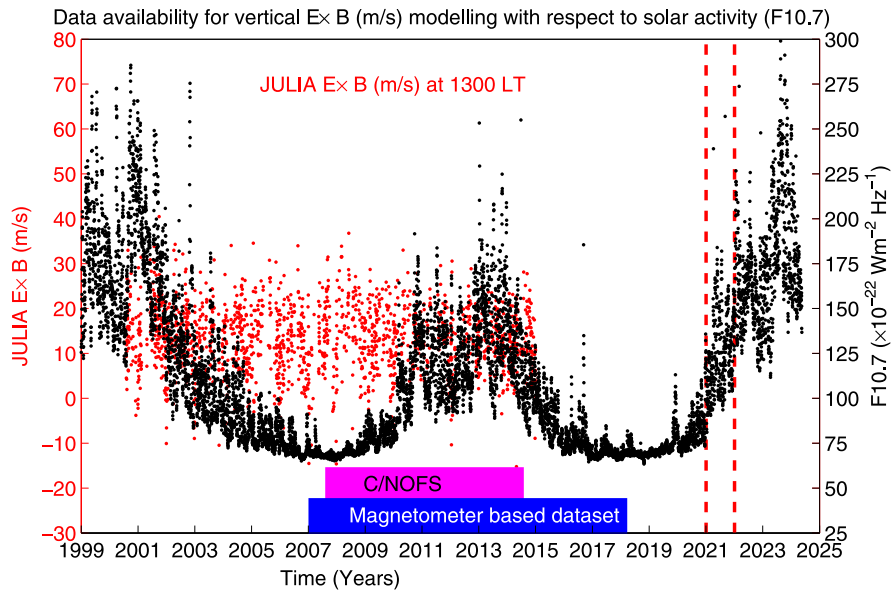

Figure 1. Solar activity (represented by F10.7 as black dots) coverage of Jicamarca JULIA vertical drifts at 13 LT (red dots), C/NOFS (purple bar) and ground-based magnetometer (blue bar) data sets used in developing the climatological vertical **E** × **B** drift model. The vertical red dashed lines indicate the time period (2022) used for model validation. The ticks on the *x*-axis are indicated at year end. For example, the end of 2021 is also the start of 2022.

(compared to other algorithms) and ability to avoid overfitting and by-pass the cross-validation step which slows down the training process (for example, Burden & Winkler, 2008), our training procedure utilized the Bayesian regularization backpropagation training algorithm (MacKay, 1992). The Bayesian Regularization algorithm allows the utilization of the entire available data set for training in problems where there is limited data, which turned out to be advantageous in our case. In this work, we use the MATLAB's Neural Network Toolbox (Matlab 2022a) and train the network using the "trainbr" function which applies the Levenberg-Marquardt optimisation as the gradient descent algorithm along with the rest of the default values. The model design followed a standard input-hidden-output layer formulation with similar hyperbolic tangent sigmoid transfer function as the preferred activation function (to enable the neural network learn the non-linearity of the problem) for input-hidden and hidden-output layers.

2.3. Relating Magnetometer Derived EEJ (ΔH) to C/NOFS Vertical E × B Drift

We first implement a relationship between magnetometer derived ΔH (EEJ) and C/NOFS vertical **E** × **B** drift over different longitude sectors during local daytime. This is accomplished through input-output non-linear mapping process embedded in artificial neural networks. Conventionally, modeling using neural networks involves splitting the data set into training, testing, and validation data sets. The training data set is used in the learning relationship between inputs and target while the testing data set ensures that the neural network generalizes as opposed to memorization during training. The validation data set is used to evaluate the learning performance of the neural network model while optimizing hyperparameters. In this study, we have followed a different approach guided by the data availability for our input-output mapping between EEJ (ΔH) to C/NOFS vertical **E** × **B** drift. Table 1 shows that magnetometer data distribution in different longitude sectors is unbalanced. Following the conventional methodology of data splitting into training, validation and testing data sets would compound the unbalanced data problem and be disadvantageous in our case. Due to this, we have adopted to use Bayesian regularization training algorithm that allows us to utilize all the available data for training for two main reasons. Neural networks that use Bayesian regularization avoid being overtrained and overfitted because the process involves Bayesian criteria for halting training and the network is only trained on effective weights ignoring irrelevant network parameters (Burden & Winkler, 2008). Furthermore, Bayesian regularization is more robust compared to traditional backpropagation neural networks with additional advantage of by-passing the cross-validation step allowing more data to be used during training. In broad terms, cross validation is also computationally intensive and consumes more time during the training process. After deciding on the neural

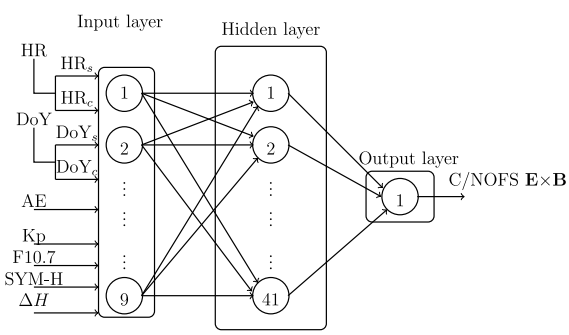

(a) Mapping procedure between ΔH (EEJ) and C/NOFS vertical $\mathbf{E} \times \mathbf{B}$ drift

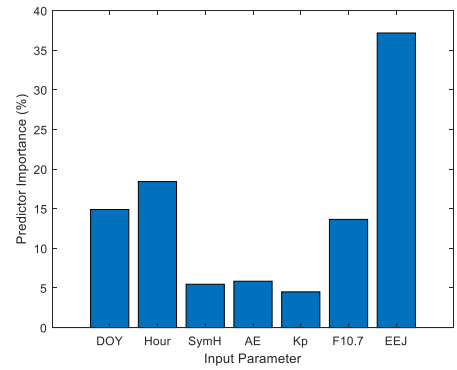

(b) Input predictor influence on vertical $\mathbf{E} \times \mathbf{B}$ drift

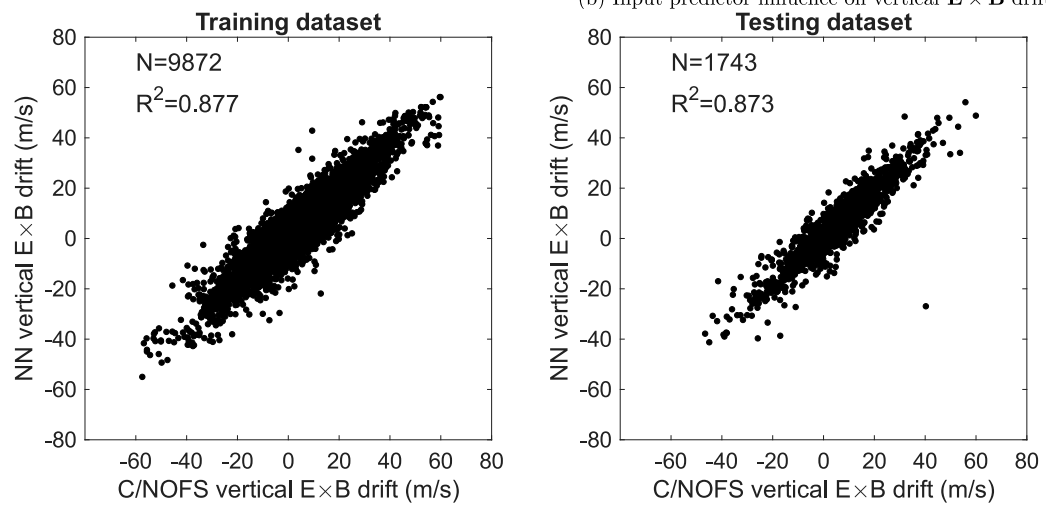

(c) Neural network performance on training and testing datasets

Figure 2. (a) Procedure followed relating magnetometer derived ΔH (EEJ) and C/NOFS vertical $\mathbf{E} \times \mathbf{B}$ drift over Jicamarca during 2008–2015 for local daytime (0700–1700 LT), (b) contribution of different inputs within the mapping process, and (c) Neural network performance on the training and testing data sets when relating EEJ (ΔH) and C/NOFS vertical $\mathbf{E} \times \mathbf{B}$ drift during 2008–2015.

network format to relate EEJ (ΔH) and C/NOFS vertical $\mathbf{E} \times \mathbf{B}$ drift, the next step is to assemble the input space (akin to independent variables in regression modeling). It has been quantitatively shown that EEJ (ΔH) is directly related to vertical $\mathbf{E} \times \mathbf{B}$ drift (for example, Anderson et al., 2004). In the ionospheric E region, the EEJ has a direct relationship with ionospheric conductivity and maximum electron density which are all influenced by the ionizing radiation. It therefore follows that in any quantitative studies and modeling of vertical $\mathbf{E} \times \mathbf{B}$ drift, solar activity is an important input. Vertical $\mathbf{E} \times \mathbf{B}$ drift exhibits strong diurnal variations and is significantly influenced by geomagnetic conditions (Fejer et al., 1979; Anderson et al., 2004). Seasonal and solar activity dependence of the F2 region vertical drifts has been previously described by Fejer et al. (1979). The EEJ along with geophysical parameters comprising solar flux (F10.7), seasonal representation, magnetic activity (SYM-H, AE and Kp) and diurnal variation form the input space with C/NOFS vertical $\mathbf{E} \times \mathbf{B}$ drift as the target parameter. This was done separately for each magnetometer pair that satisfied the criteria for estimating EEJ. For demonstration purposes, Figure 2a shows the input-output mapping setup relating magnetometer derived ΔH (EEJ) to C/NOFS vertical $\mathbf{E} \times \mathbf{B}$ drift over Jicamarca covering 2008–2015 for local daytime (0700–1700 LT). The inputs have different time resolutions. AE, SYMH and ΔH (EEJ) have 1 min temporal resolution while DoY remain the same for the entire day. F10.7 has one daily value and Kp is a 3 hr index. In Figure 2, data is considered in its format. For example, for DoY 1, if data for all inputs existed, F10.7 is a constant value, Kp is repeated for every 3 hr, while AE, SYMH and EEJ maintain their high resolution at 1 min after converting the time to full hour. The output/target parameter is C/NOFS vertical $\mathbf{E} \times \mathbf{B}$ drift that has been averaged over 1 min resolution.

In Figure 2a, the day number of the year (DoY) and hour of the day (HR) represent seasonal and diurnal variations of vertical $\mathbf{E} \times \mathbf{B}$ drift and were split into their respective cyclic components (for example, Poole & McKinnell, 2000) as follows

$$DoY_s = \sin\left(\frac{2\pi \times DoY}{365.25}\right), DoY_c = \cos\left(\frac{2\pi \times DoY}{365.25}\right) \quad (1)$$

$$HR_s = \sin\left(\frac{2\pi \times HR}{24}\right), HR_c = \cos\left(\frac{2\pi \times HR}{24}\right) \quad (2)$$

Where DoY_s and DoY_c are the sine and cosine components of DoY, and HR_s and HR_c are the sine and cosine components of HR. Training is performed while monitoring the root mean square error (RMSE) on the testing data set. The number of hidden neurons with the lowest RMSE was determined as 41 in Figure 2a.

Three magnetic indices; symmetric component of the ring current (SYM-H), auroral electrojet (AE) and planetary Kp were considered to describe the dependence of vertical $\mathbf{E} \times \mathbf{B}$ drift on geomagnetic conditions. We determined the relative contribution of input features by subjecting the input-output space to a regression model based on bootstrapping algorithm with decision trees approach using a built-in "fitrensemble" Matlab function. The predictor importance is then estimated using the "predictorimportance" Matlab function through the permutation of different inputs followed by computation of prediction error when each input is included. Figure 2b demonstrates the predictor importance of each input highlighting that magnetometer derived ΔH contributes over 35% to C/NOFS vertical $\mathbf{E} \times \mathbf{B}$ drift variability over Jicamarca during 2008–2015, followed by seasonal and diurnal variations which account for a combined influence of about 33%. While the individual contribution of each magnetic index is around 5%, usage of all the three indices account for ~17% of vertical $\mathbf{E} \times \mathbf{B}$ drift changes. The higher contribution of ΔH to the modeling process is physically expected since the perpendicularity of equatorial eastward electric field (that initiates the EEJ generation) with geomagnetic field results into vertical $\mathbf{E} \times \mathbf{B}$ drift. The solar activity indicator F10.7 shows a feature importance of about 14%. Its contribution is linked to solar activity's role in influencing the E region which plays a major role in EEJ. As established, ΔH is directly related to EEJ that is proportional to the product of ionospheric conductivity and eastward electric field (Anderson et al., 2004). Conductivity is related to maximum electron density in the E region which is primarily determined by the strength of the ionosing radiation during local daytime. Based on results of Richmond (1973) which reported a simultaneous increase of 10% in both ΔH and maximum electron density of the E region, and findings of Fejer et al. (1979) showing variability of vertical drifts with different solar activity periods, F10.7 was included as an input in the modeling. The low contribution of geomagnetic inputs is related to the amount of disturbed data within the entire database used for modeling. It is known that the network may not learn the behavior of ionospheric variability related to extreme events as there are few examples presented during training. Figure 2c shows model's performance on both training and testing data sets while relating EEJ (ΔH) and C/NOFS vertical $\mathbf{E} \times \mathbf{B}$ drift over different magnetometer locations during 2008–2015. The coefficient of determination (R^2) values for the training and testing data sets are nearly identical with a difference of 0.004 indicating that the model achieved generalization with little probability of overfitting or overtraining. Due to non-continuity of the C/NOFS satellite data, the resulting relationship needs to be validated. Although, the C/NOFS satellite data are non-continuous over a single magnetometer location, once the relationship is established, the coefficients can be used to generate vertical $\mathbf{E} \times \mathbf{B}$ drift at the time when daytime EEJ data are available. Figure 3a shows the magnetometer locations over which EEJ was determined using the differential magnetometer method (Anderson et al., 2004). For details of the magnetometer locations off the equator, the reader is referred to Table 1. Direct subtraction of the geomagnetic H component observations at the equator from corresponding data set at the magnetometer location off the equator provides the changes in H component (ΔH) which is directly proportional to vertical $\mathbf{E} \times \mathbf{B}$ drift during local daytime (Anderson et al., 2004; Yizengaw et al., 2014). The approach is unsuitable during local nighttime because the currents are too weak to be detected by ground-based magnetometers. Based on the procedure in Figure 2, vertical $\mathbf{E} \times \mathbf{B}$ drifts over each magnetometer location in Figure 3a are determined for periods in Table 1 when magnetometer data was available. This approach requires validation with an independent data set. To validate the proposed methodology, Figure 3b illustrates the comparison between observed (JULIA measurements) and reconstructed vertical $\mathbf{E} \times \mathbf{B}$ drifts over Jicamarca (11.8°S, 77.2°W) in 2009 and 2013 representing periods of low and high solar activity, respectively. Results show that the correlation (R) value between reconstructed and JULIA vertical $\mathbf{E} \times \mathbf{B}$ drift is almost similar ($R = 0.73$) for 2009 and 2013. Previously,

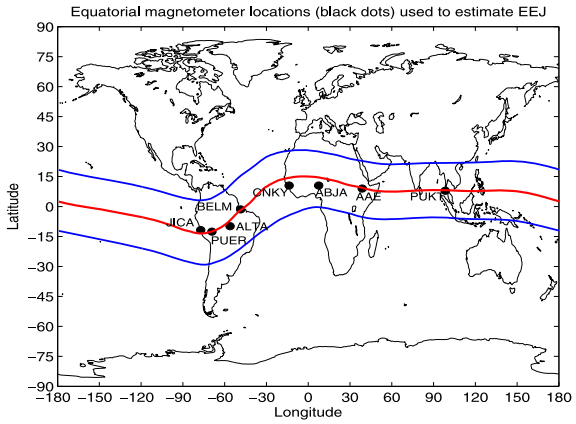

(a) Magnetometer stations used to compute EEJ

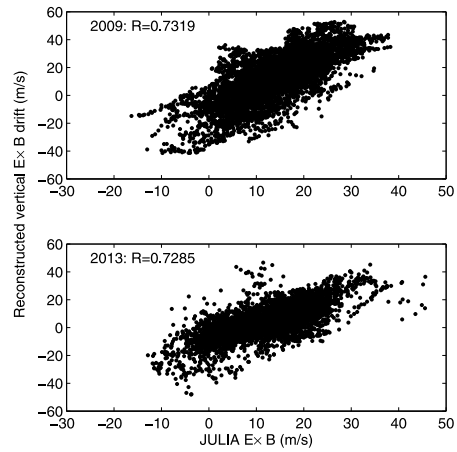

(b) Observed and reconstructed vertical $\mathbf{E} \times \mathbf{B}$ drifts over Jicamarca

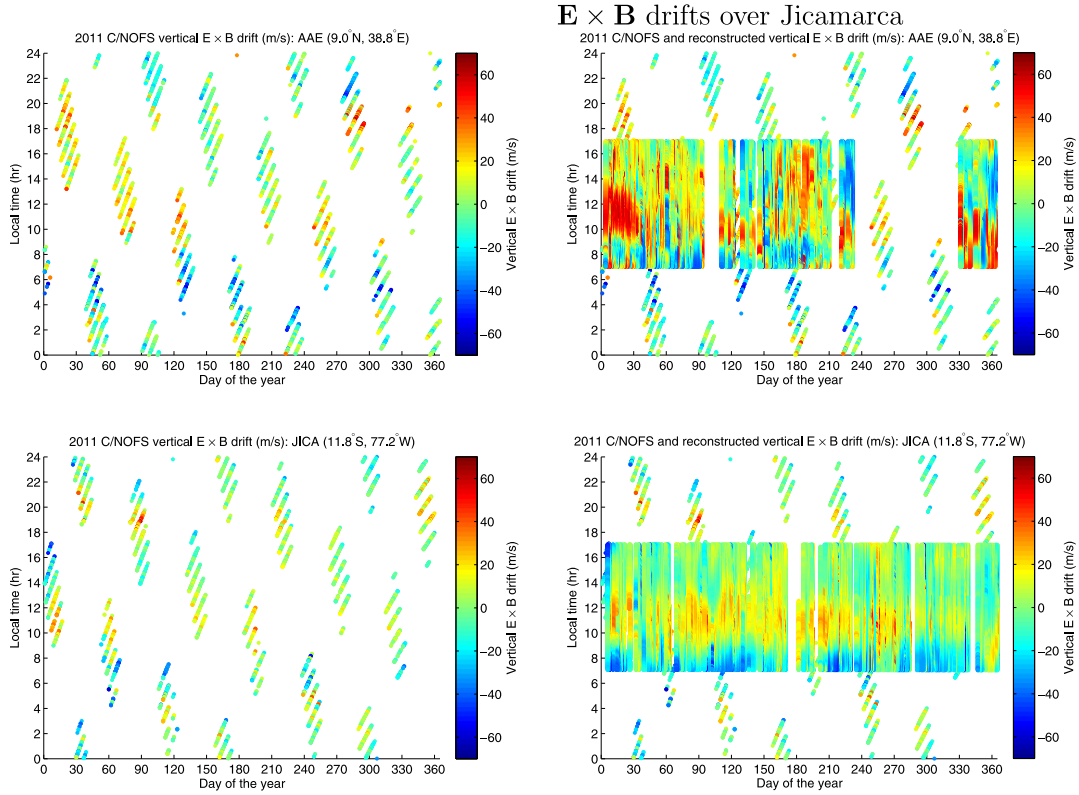

(c) C/NOFS vertical $\mathbf{E} \times \mathbf{B}$ drift over AAE and JICA (first column) and when magnetometer derived drifts are superimposed during local daytime (second column) in 2011.

Figure 3. (a) Equatorial magnetometers used to calculate EEJ, and (b) comparison between reconstructed and observed vertical $\mathbf{E} \times \mathbf{B}$ drifts in 2009 and 2013 over Jicamarca. For details of all magnetometer locations, see Table 1. Panels in (c) demonstrate C/NOFS vertical $\mathbf{E} \times \mathbf{B}$ drift over AAE and JICA (first column) and when magnetometer derived vertical $\mathbf{E} \times \mathbf{B}$ drifts are superimposed (second column) in 2011.

Anderson et al. (2004) reported R of 0.87 between JULIA vertical $\mathbf{E} \times \mathbf{B}$ drift and ΔH. Given that both JULIA drifts and ΔH are strongly influenced by E region dynamics, our R of 0.73 in both low and high solar activity periods highlights a strength of the developed relationship between ΔH and C/NOFS vertical drifts within 400–550 km. The 150 km echoes and magnetometer derived vertical $\mathbf{E} \times \mathbf{B}$ drift are dominated by E-region processes, while the ISR drifts altitudinal range is about 250–600 km (Scherliess & Fejer, 1999). The vertical ion plasma drift from C/NOFS were limited within 400–550 km. While the altitude ranges of the data combined to develop

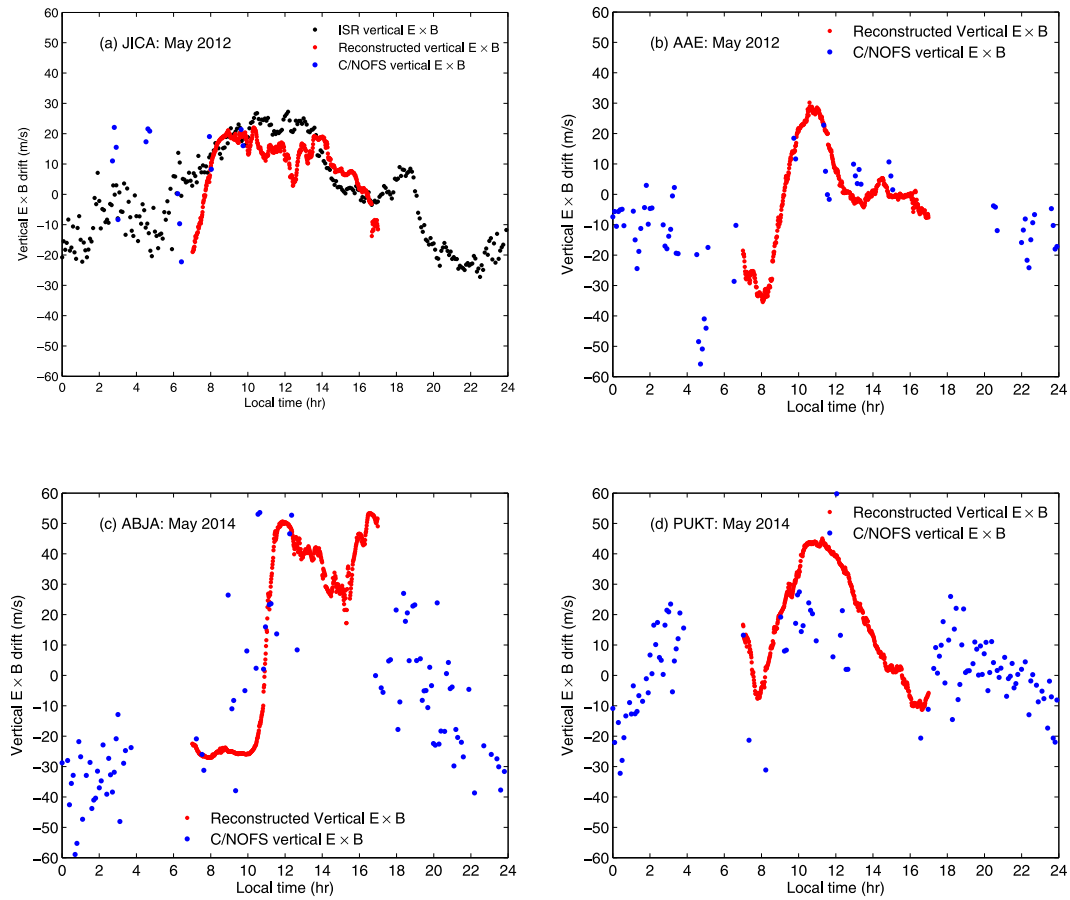

Figure 4. Monthly median reconstructed and observed vertical **E** × **B** drifts in May 2012 over (a) Jicamarca JICA (11.8°S, 77.2°W), (b) Addis Ababa AAE (0.8°N, 38.8°E), and in May 2014 over (c) Abuja ABJA (8.99°N, 7.38°E) and (d) Phuket PUKT (7.9°N, 98.4°E). Black, blue and red dots represent ISR, C/NOFS and reconstructed vertical **E** × **B** drifts, respectively.

the model are different, the altitudinal changes in vertical **E** × **B** drift have been shown to be small (Shidler & Rodrigues, 2020) and conclusions derived from this study are not expected to be significantly influenced on a long-term scale. Once the relationship between non-continuous C/NOFS vertical **E** × **B** drift and ΔH has been established following the approach in Figure 2a, a relatively "continuous" vertical **E** × **B** drift database can be reconstructed at each time when ΔH is available. To demonstrate the outcome, Figure 3c shows C/NOFS vertical **E** × **B** drift over AAE and JICA (first column) and when magnetometer derived vertical **E** × **B** drifts are superimposed (second column) in 2011 during local daytime. As can be seen, the advantage of this approach is to increase the data resolution of vertical **E** × **B** drift in different longitude sectors during periods of magnetometer observations.

Figure 4 shows the benefit of the methodology in reconstructing daytime vertical **E** × **B** drift over (a) Jicamarca JICA (11.8°S, 77.2°W), (b) Addis Ababa AAE (0.8°N, 38.8°E), (c) Abuja ABJA (8.99°N, 7.38°E) and (d) Phuket PUKT (7.9°N, 98.4°E). ISR, C/NOFS and reconstructed vertical **E** × **B** drifts are plotted in black, blue and red dots, respectively. Figures 4a–4d are monthly median vertical **E** × **B** drift values for May 2012 and 2014, respectively. Due to different locations, it is difficult to find a common period with sufficient data for computation of monthly median vertical **E** × **B** drift data. Of all locations in Figure 4, only JICA has ISR data set. Nevertheless, Figure 4a demonstrates that the reconstructed vertical **E** × **B** drift follows the climatological drifts from the ISR in May 2012, a result that is assumed to be consistent over all magnetometer locations in this study. It should be highlighted that the monthly median ISR vertical **E** × **B** drift is computed from available data for few days 22–25 May 2012. For direct comparison, reconstructed and C/NOFS vertical **E** × **B** drift are also shown for 22–25 May 2012 over JICA. Figures 4a–4d highlight the continuity in monthly median vertical **E** × **B** drift during local daytime (with respect to C/NOFS drifts, plotted in blue dots) as a result of data reconstruction.

2.4. Final Vertical E × B Drift Model Development

The final model is constructed by combining available JULIA and C/NOFS data sets as well as the reconstructed vertical **E** × **B** drift data at different longitudes (see Figure 3a) following the previous described procedure. For the final model, C/NOFS and Δ*H* reconstructed vertical **E** × **B** drift are averaged at 3 and 30 min, respectively to minimize potential noise in the data. The respective high resolution inputs SYMH and AE indices are averaged accordingly. The JULIA data set retains its original 5 min resolution, and relevant inputs selected at 5 min intervals. Compared to Figure 2a and with exception of Δ*H*/EEJ, the latitude and longitude are additional inputs in Figure 5a which shows the model set up. One of the most challenging problems is the determination of the optimum architecture, especially the hidden neurons responsible for input-output mapping process.

To address this, we developed several models by starting with one hidden neuron and gradually increased the number of these neurons. This was followed by validating the developed models on three different data sets by computing the RMSE between modeled and actual vertical **E** × **B** drift data. These data sets are the test data set (15%) selected randomly from the global vertical **E** × **B** drift and set aside before training, 15% testing data set, and magnetometer derived vertical drifts over Jicamarca. Figure 5b shows the RMSE values between modeled and 15% of the unseen data (removed before training, in black color), 15% randomly selected subset (testing data set) from the entire global vertical **E** × **B** drift database (blue) as well as the long-term magnetometer based derived vertical **E** × **B** data (red) for 11 year period over Jicamarca. The best model is the one that generalizes data patterns as opposed to memorization. The procedure followed guides us to identify the hidden neurons satisfying this requirement. RMSE results from the testing data set (blue curve) shows that the RMSE value from hidden neuron 70–71 reduces by 2%, and thereafter the RMSE attains relative stability starting from hidden neuron 71–78. From hidden neuron 78–79 the RMSE slightly increases by 1.5% followed by a reduction of 2.7% (neurons 79–80). This reduction of RMSE after being constant for sometime may be an indication of the network memorization. Results from the unseen (black dots) test data set (15% set aside before training) exactly mirrors this trend. We cross-reference changes in RMSE results on magnetometer derived vertical **E** × **B** drift over Jicamarca, a location chosen based on its long-term database. Results for Δ*H* derived vertical **E** × **B** drift data indicate that RMSE values were relatively constant (with very minor variations) from hidden neurons 71–78 at around 13 m/s and achieved highest reduction of 6.6% from hidden neuron 79–80 since the start of the training. This agrees with the relatively similar scenario observed from the testing data set results (blue curve) randomly selected from the global vertical **E** × **B** drift database. Thus, for model stability, we simulate vertical **E** × **B** drift for hidden neurons 71–78 (indicated by the black rectangle) and average the outputs that constitute final modeled results. In deciding the appropriate number of hidden neurons, more weight is assigned to RMSE results of the unseen test and testing data sets (black and blue curves). Here, we should emphasize that there is no straight forward method of selecting hidden neurons, and most studies consider it as a "trial and error" problem. Presented results in the next sections are based on this modeling approach. Figure 5c shows the RMSE (black dots) and *R* (red stars) results of individual models for hidden neurons 71–78 and averaged metrics highlighting the relevance of ensembling instead of selecting one model with the lowest RMSE. By performing ensembling, the RMSE and *R* reduce (increase) from average values of about 13.8 m/s (0.68) to 13.24 m/s (0.715) accounting for improvements of 4% and 5%, respectively. The *R* values for both training and testing data sets ranged from 0.680 to 0.687 and ensembling boosts the correlation to above 0.7. While this may be thought of as a low *R* value, it is significant given the complexity of the problem. The model combines different data sets namely ISR's JULIA data, magnetometer derived vertical drifts and C/NOFS drifts, all with possible different error sources based partly on their altitudes. The ensemble's *R* of 0.715 agrees with the 0.73 obtained when the relationship between C/NOFS vertical **E** × **B** drift and magnetometer derived Δ*H* was validated on JULIA observations offering additional confidence in the developed model.

3. Results and Discussion

To demonstrate the capability of the developed vertical **E** × **B** drift model, we show results over JICA, AAE and PUKT, representing American, African and Asian longitude sectors respectively during the years 2001, 2012 and 2022. For all our results, we compare with the widely used empirical vertical **E** × **B** drift model (Fejer et al., 2008) included in the IRI 2020 model (Bilitza et al., 2022). This climatology for equatorial F region vertical **E** × **B** drift was developed based on a 5 years database (July 1999 to June 2004) from the Ionospheric Plasma and Electrodynamics Probe Instrument (IPEI) onboard ROCSAT-1 satellite (Fejer et al., 2008). In contrast, results presented in this paper are based on diverse data sets from different instruments. Magnetometer data cover 6–12,

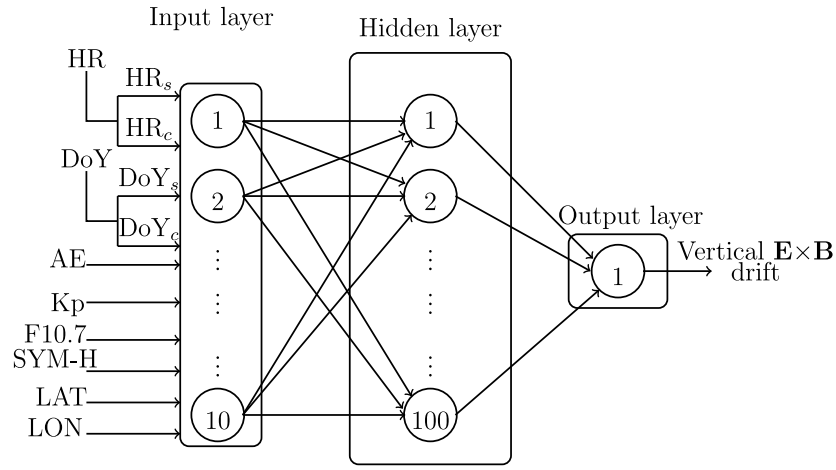

(a) Overall vertical $\mathbf{E} \times \mathbf{B}$ drift model set up

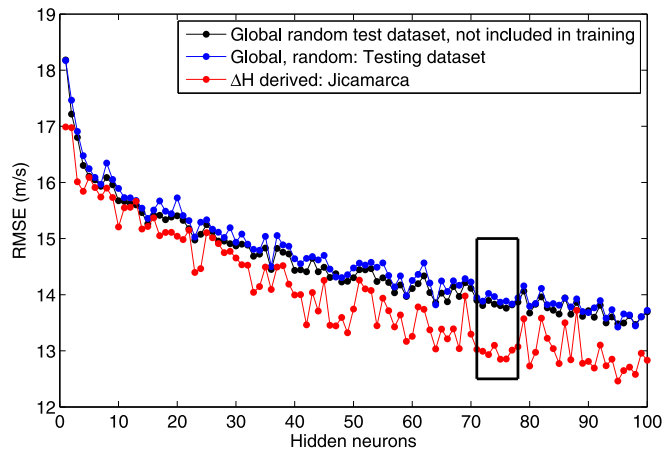

(b) RMSE values for different models

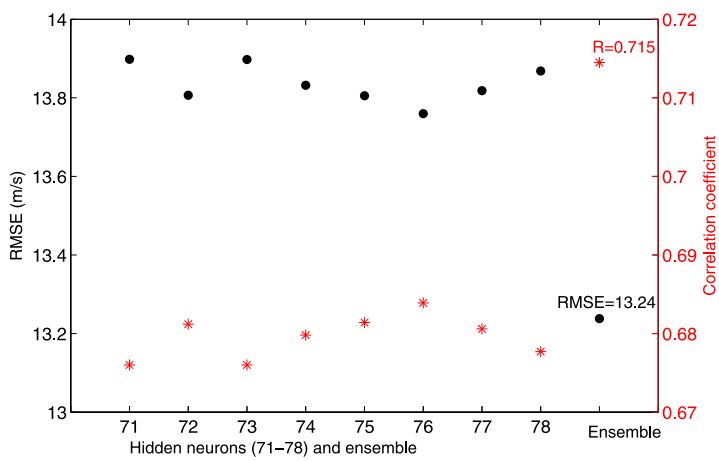

(c) RMSE, correlation and ensemble results for hidden neurons 71-78

Figure 5. (a) Global vertical $\mathbf{E} \times \mathbf{B}$ drift model set up, (b) RMSE values for different hidden neurons during the determination of the optimum architecture, and (c) ensembling results for hidden neurons 71–78. The black rectangle shows neurons 71–78 used in simulating final vertical $\mathbf{E} \times \mathbf{B}$ drift data.

10.1029/2025EA004622

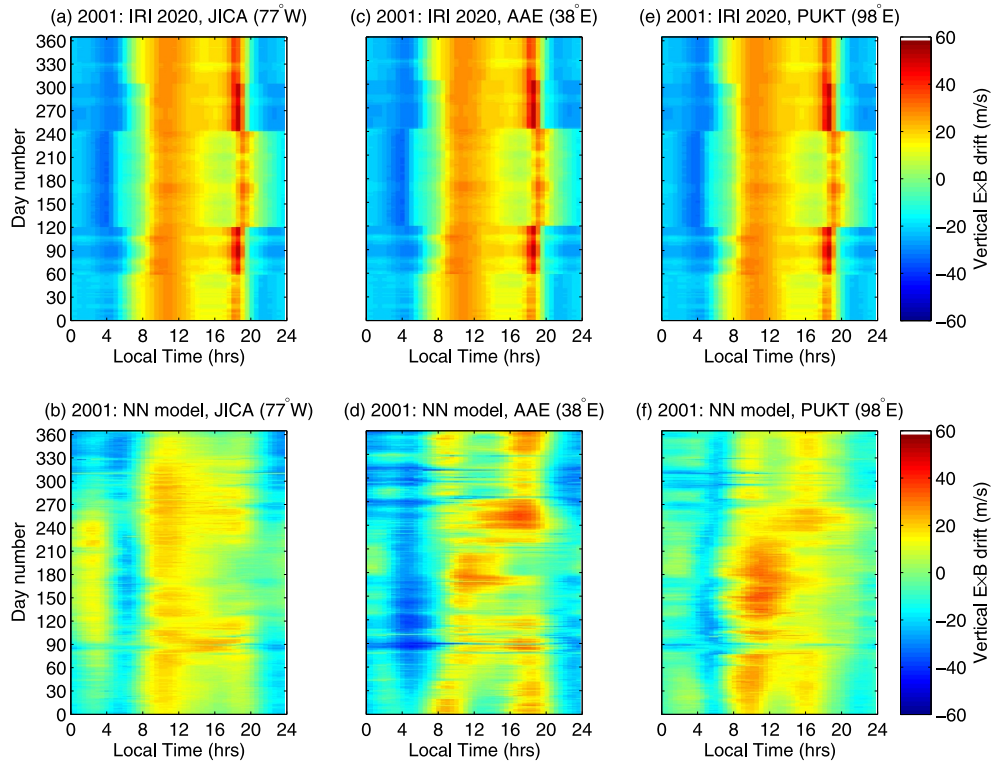

Figure 6. Modeled vertical **E** × **B** drifts in 2001 over (a, b) Jicamarca JICA (11.8°S, 77.2°W), (c, d) Addis Ababa AAE (0.8°N, 38.8°E), and (e, f) Phuket PUKT (7.9°N, 98.4°E). The top row shows IRI 2020's results and the bottom row refers to the proposed model.

5–7 and 3 years over the American, African and Asian sectors, respectively, while C/NOFS global data set ranges from 2008 to 2015. The American sector is perhaps "over-represented" with an additional JULIA data set from 2001 to 2015. Our neural network model (hereafter referred to as NN) therefore covers a significant range of solar flux levels compared to existing approaches. Because we have implemented the Fejer model (Fejer et al., 2008) incorporated within the IRI model platform, we shall refer to its outputs as the IRI 2020 hereafter throughout the paper.

Figures 6–8 show the comparison of the NN and IRI-2020 vertical **E** × **B** drift models over JICA, AAE and PUKT for 2001, 2012 and 2022, respectively. Both models show that daytime peak vertical **E** × **B** drift values occur between 9 and 12 LT. Distinct observations from these figures include the fact that over all longitude sectors, the IRI 2020 model provides a stronger PRE compared to the NN model. The newly developed model provides higher drift values between 0 and 4 UT and this is more pronounced for JICA. This seems to correlate with solar flux levels as modeled vertical **E** × **B** drift magnitudes during this time interval are higher in 2001 (maximum F10.7 = 285 sfu) followed by 2022 ($F10.7_{max}$ = 257 sfu) compared with maximum F10.7 of 183 sfu in 2012. Figure 6 shows that in 2001, the IRI 2020 model gives PRE that is higher than daytime drifts in the three longitude sectors. The NN model clearly agrees with the IRI 2020 model only over the African sector. A common feature about Figures 6–8 is the observation of higher NN modeled vertical **E** × **B** drift values over the Asian sector compared to the African and American sectors, an observation that is consistent to findings reported in Yizengaw and Groves (2018). Additionally, the local time vertical drifts behavior with respect to seasons from the IRI 2020 is nearly identical irrespective of the longitude sector, but there are small amplitude differences reaching about 5 m/s. Due to lack of measured continuous temporal observations, it is difficult to interpret Figures 6–8 in terms of vertical **E** × **B** drifts magnitudes. However, looking at Figures 1 and 3b, it is clear that modeled vertical **E** × **B** drift values are to a large extent in agreement with observed values within −20 to 40 m/s over Jicamarca. This aspect is investigated further in the next section. In Figures 6–8, the NN model generates upward vertical drifts during about 0–4 LT over Jicamarca. This is an intriguing result given that it is predominantly over Jicamarca compared to the African and Asian sectors. It is possible that being empirical, this result may be attributed

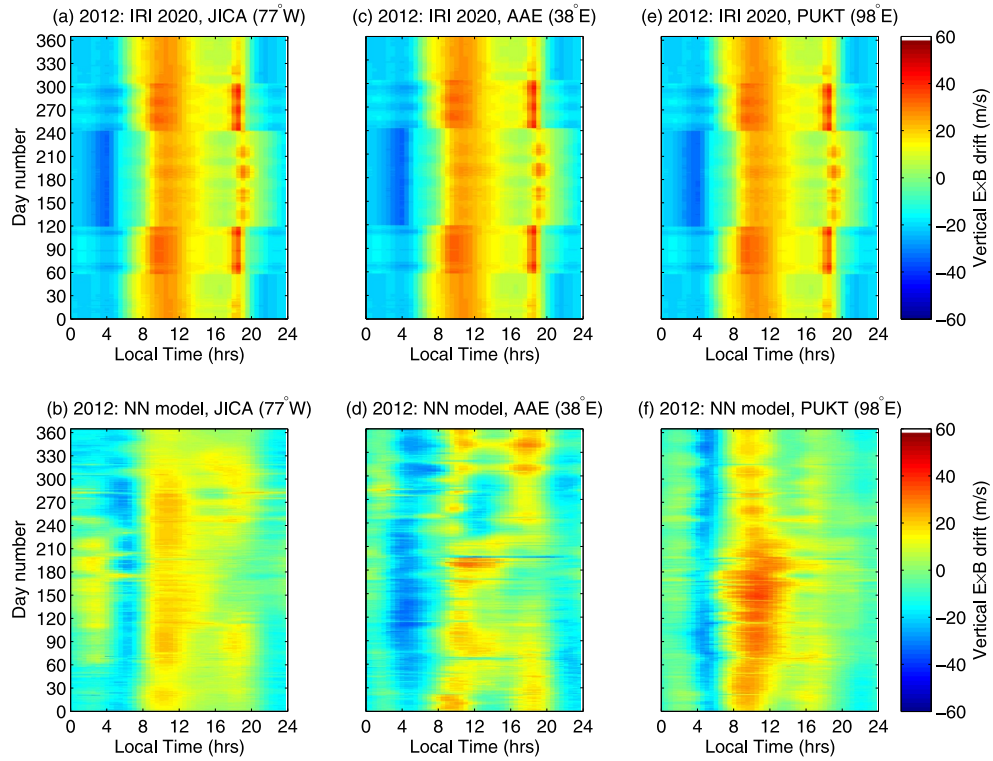

Figure 7. Similar to Figure 6 for 2012.

to C/NOFS data used in model development which exhibited upward plasma drift in the post midnight sector (for example, Fang et al., 2016). Post midnight upward vertical drifts are more pronounced in 2001 NN modeled results shown in Figure 6. From the data distribution with respect to solar activity (Figure 1) used in model development, C/NOFS observations are available during solar activity phases that were lower than the high solar activity period represented by 2001. Thus, during high solar activity periods, the current NN model may be yielding slightly higher post midnight vertical drifts reflected in C/NOFS data. Plasma drifts during low solar activity (such as 2008–2010 covered by C/NOFS data in model development) could easily be influenced by other factors such as thermospheric dynamics related with midnight temperature maximum (for example, Fang et al., 2016) and/or lower atmospheric waves in comparison to plasma drifts in high solar activity periods. Additionally, it is possible for system biases in C/NOFS's IVM drifts data associated with low solar activity periods. Previously, Fang et al. (2016) observed midnight upward vertical drifts from C/NOFS measurements and investigated this further using the Whole Atmosphere Model coupled with Global Ionosphere Plasmasphere model in June–July and November–December 2010 simulations at 500 km altitude. Their results successfully reproduced the midnight upward vertical drifts during 0–3 LT, an observation that was clearer within about 60−120°W longitude sector and attributed to thermospheric dynamics associated with midnight temperature maximum (Fang et al., 2016). Recently, Chou et al. (2023) studied the day-day variability of midnight equatorial plasma bubbles using SAMI3 and SD-WACCM-X models, and reported upward vertical drifts at around 0 LT and 01 LT at about 60−120°W longitudes (see their Figure 4). They remarked that "the westward wind associated with the solar terminator waves and gravity waves induces polarization electric fields that map to the equatorial ionosphere from high latitudes, resulting in midnight vertical drift enhancement." We have further simulated NN vertical drifts within $\pm 5^0$ latitude around the geomagnetic equator for day of year 165 in 2005, 2010, 2015 and 2020 at 02 LT (average of 0–4 LT when upward vertical drifts are seen in Figures 6–8 over Jicamarca) and results are shown in Figure 9. Results in Figure 9 show that the longitude sector covering Jicamarca shows upward vertical drifts within $\pm 5^0$ latitude irrespective of the year, while most of the African sector is dominated by downward midnight vertical drifts. It therefore appears that upward midnight vertical drifts reproduced by our NN model are possible. However, given that this appears to be stronger over the American longitude sector, this

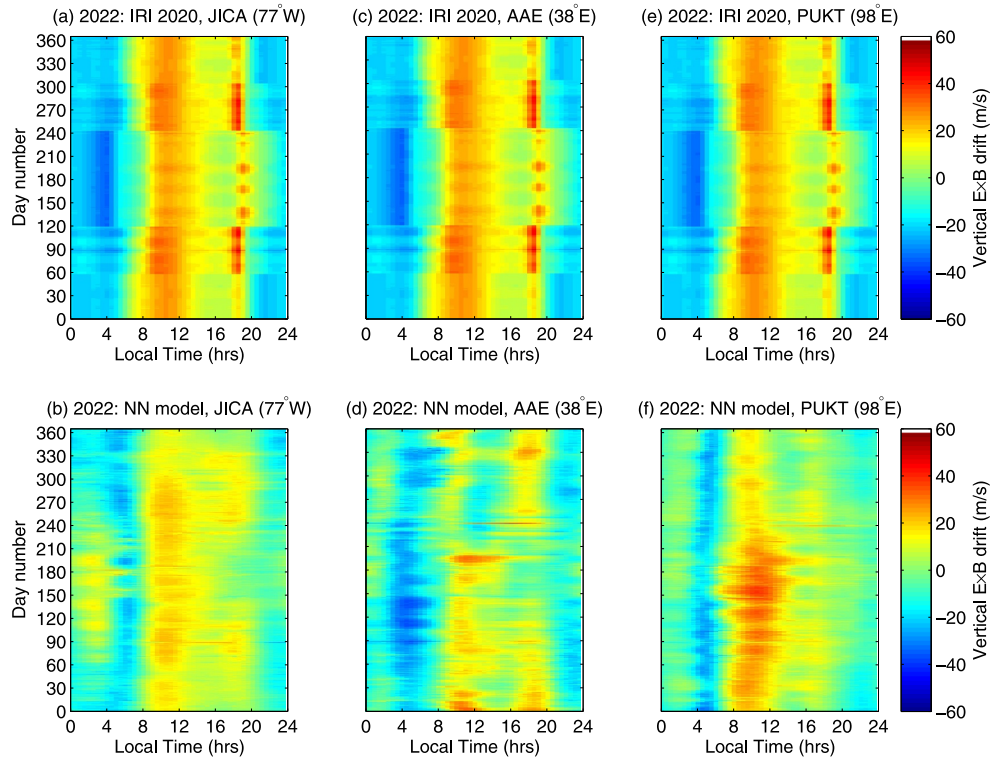

Figure 8. Similar to Figure 6 for 2022.

requires a further investigation and particularly an extensive validation of the developed NN model with actual data in all longitude sectors.

3.1. Comparison With ICON IVM Vertical E × B Drifts

Figure 10 shows a comparison between IVM vertical **E** × **B** drifts and modeled values provided by the IRI 2020 and NN models over the American, African and Asian sectors represented by JICA, AAE and PUKT, respectively for 2022.

IVM plasma drifts are selected based on the high quality data flag $ICON\_L27\_RPA\_Flag = ICON\_L27\_DM\_Flag = 0$ (for example, Harding et al., 2025; Zhang et al., 2024). IVM data set is considered within magnetic latitudes of ±7.5° (Hysell et al., 2023) and ±7° geographic longitudes, respectively over JICA, AAE and PUKT. The resulting data set is further categorized (according to the southern hemisphere) into January – February (summer), March – April (equinox) and May – August (solstice). Each season's IVM drifts (within ±150 m/s) are binned and averaged by local time resolution of 90 min. The binning temporal resolution of 90 min is chosen because the satellite orbital period is about 1.5 hr. Results of this procedure are plotted as black dots in Figure 10. A similar procedure is applied to NN and IRI 2020 modeled data, and corresponding monthly average vertical **E** × **B** drifts plotted in blue and red colors respectively. The year 2022 is selected for this comparison because prior to this, the IVM ion drift observations were inaccurate due to light ion contamination linked to low solar flux levels (Hysell et al., 2024). The large variability of IVM plasma drifts in Figure 10 around 4–8 LT is linked to its relatively low quality in the morning sector compared to other local times (for example, Zhang et al., 2024).

The developed model in this study utilized data until 2019 and the comparison in 2022 is therefore performed on a completely independent data set both in time and from a different source that was not included in the model development. Based on Figure 10, a few observations can be made regarding the performance of the existing IRI 2020 climatological model and the newly developed approach

- Where a clear pattern exists, the IRI 2020 model provides higher PRE than IVM data over all sectors. This observation has also been mentioned recently (for example, Hysell et al., 2024) while comparing IVM

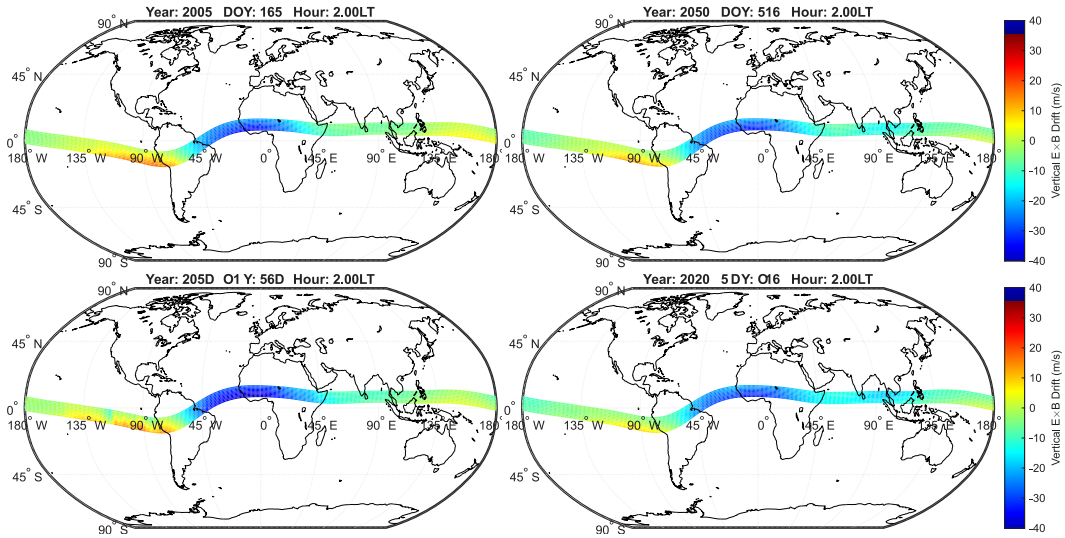

Figure 9. NN modeled vertical **E** × **B** drift for day 165 in 2005, 2010, 2015 and 2020 at 2 LT.

observations with the established climatology. PRE overestimation by the IRI model has recently been reported over the African sector (Cesaroni et al., 2025). In this context, our model consistently reproduces a lower PRE in comparison with the established climatology (Fejer et al., 2008) and is closer to IVM drifts in some cases.

- Our climatological results show that higher drifts appear over the Asian sector compared to African and American sectors. This is consistent across the three investigated seasons in 2022. Both Figures 8 and 10 confirm this. This is an aspect that requires further investigation especially our model's validations with independent data sets.
- Our results show that there is no clearly pronounced PRE in May–August solstice season. Coincidentally, available IVM drift data tend to agree with this modeled result. Confirmation of this observation requires more detailed investigation using observed data, rather than relying on models. We note that the established IRI 2020 climatology yields a clear PRE during this season over all sectors.

RMSE results for data in Figure 10 show that the NN model yields lower and higher RMSE over the American and Asian sectors, respectively across all seasons. Being an empirical model, it is strongly influenced by the amount of data used in its development over certain regions. The performance of IRI 2020 and NN models is comparable during January – February and March – April over the Asian sector. Using RMSE values for IRI and NN models, we compute percentage improvement of the NN model over IRI in estimating IVM vertical drift using:

$$\text{improvement} = \left(\frac{\text{RMSE}_{\text{IRI}} - \text{RMSE}_{\text{NN}}}{\text{RMSE}_{\text{IRI}}}\right) \times 100\%. \quad (3)$$

We then average the improvement values over all seasons for each longitude sector to obtain the percentage performance of the NN model over the IRI model that is taken as the existing climatology. The improvements in terms of estimating IVM drifts over the existing climatology representation are about 40%, 22% and 7% over the American, African and Asian sectors, respectively across the entire 2022 data set considered in Figure 10. In simple terms, the NN model's accuracy in estimating ICON IVM's vertical drifts is in the range of 7%–40% better than the IRI 2020 model. It is important to stress that this deduction is made based on climatological IVM data within ±7.5° magnetic equator and ±7° longitude of JICA, AAE and PUKT locations which represent different longitude sectors. Given that this is an empirical model, the NN model's performance is likely to be influenced by the amount of data used in its construction. For example, the magnetometer derived vertical **E** × **B** drifts over the American sector covered up to 12 years over different locations spanning a 20° longitude range in comparison with about 7 years for the African sector. The Asian sector is the least represented with 3 years over a single location. The reader is referred to Table 1 for details about data coverage in the three longitude sectors.

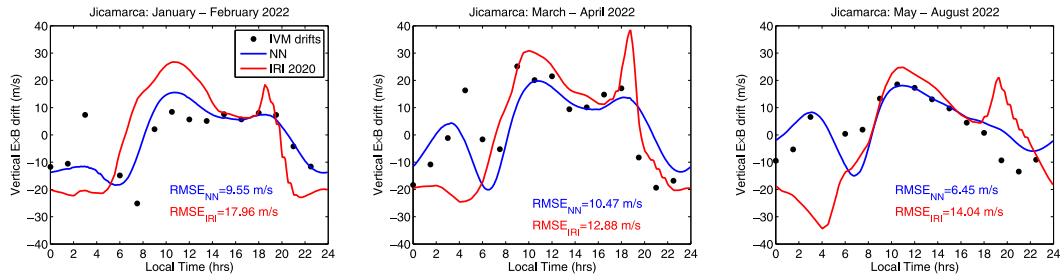

(a) IVM (black dots), NN (blue) and IRI 2020 (red) vertical $\mathbf{E} \times \mathbf{B}$ drifts over Jicamarca (11.8°S, 77.2°W) in 2022

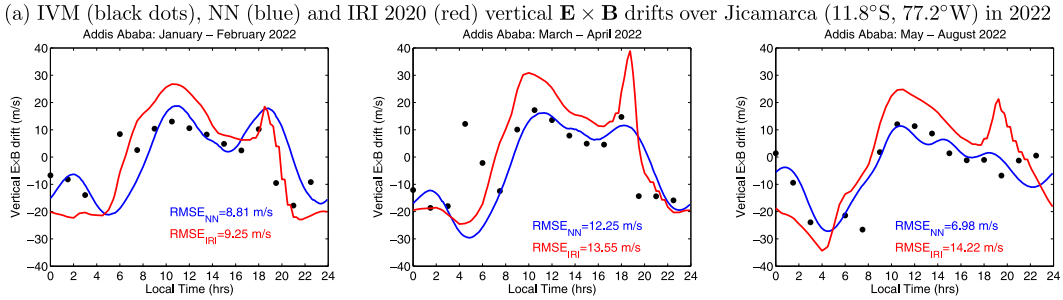

(b) IVM, NN and IRI 2020 vertical $\mathbf{E} \times \mathbf{B}$ drifts over Addis Ababa (9.0°N, 38.8°E) in 2022

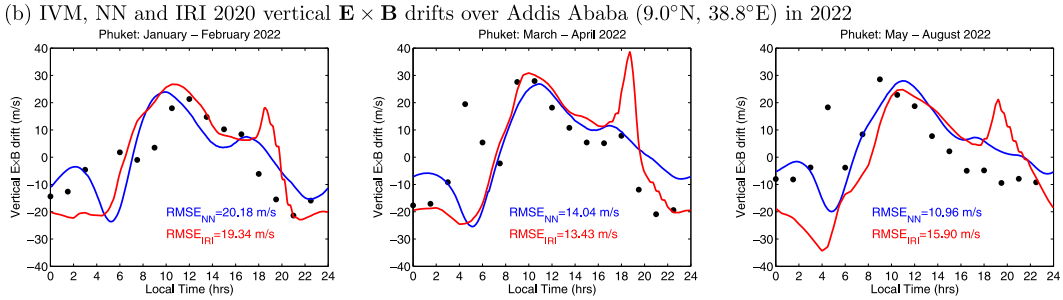

(c) IVM, NN and IRI 2020 vertical $\mathbf{E} \times \mathbf{B}$ drifts over Phuket (7.9°N, 98.4°E) in 2022

Figure 10. Comparison of IVM vertical $\mathbf{E} \times \mathbf{B}$ drifts with the developed NN and IRI 2020 models over the (a) American, (b) African, and (c) Asian sectors in 2022.

4. Conclusions

A new global climatological vertical $\mathbf{E} \times \mathbf{B}$ drifts model has been developed over low latitude regions using a combination of satellite, radar and ground-based observations. A major contributing factor employed was to derive daytime $\mathbf{E} \times \mathbf{B}$ drifts by mapping magnetometer derived EEJ to C/NOFS vertical drifts in different longitude sectors. This enabled us to include detailed longitudinal $\mathbf{E} \times \mathbf{B}$ drift variability in model development. As a result, the new model appears to show more details in vertical $\mathbf{E} \times \mathbf{B}$ drifts compared to the existing established climatology. Based on IVM drifts for January – August 2022, the NN model is more accurate over the American longitude sector, an observation that is clearly linked to the amount of data and its duration that was included in the empirical approach. The NN model more closely represents the climatology of ICON IVM'vertical drift over the existing model by 7%–40% in different geographic longitude regions, highlighting that overall, it improves the F-region climatology representation. We plan to make this model publicly available for extensive validation with various data sets at all longitude sectors.

Conflict of Interest

The authors declare no conflicts of interest relevant to this study.

Availability Statement

EEJ data is available at https://sites.bc.edu/magnetometers/downloads. AMBER is operated by The Aerospace Corporation and Boston College with funding from NSF and AFOSR. SAMBA is also operated by UCLA and funded by NSF. C/NOFS satellite is publicly available from https://cdaweb.gsfc.nasa.gov/. The Dst and Kp

indices data were accessed from the World Data Centre, Kyoto, Japan http://wdc.kugi.kyoto-u.ac.jp. The IRI 2020 model is available on http://irimodel.org/. F10.7, AE and SYM-H indices are available from https://omniweb.gsfc.nasa.gov/form/dx1.html. ISR data is accessible via https://www.igp.gob.pe/observatorios/radio-observatorio-jicamarca/madrigal/. ICON IVM data is publicly available from https://icon.ssl.berkeley.edu/Data. This work uses version 8 revision 2 (v08r002) of the IVM drift data that has been corrected for offsets in ion drifts in the instrument frame (https://icon.ssl.berkeley.edu/news/new-ivm-data-v08r002-now-available).

Acknowledgments

This work is based on the research supported in part by the National Research Foundation of South Africa (Grant 112090 and 129285) and opinions, findings and conclusions or recommendations expressed in this paper are of the author(s), and the NRF accepts no liability whatsoever in this regard. Contributions of MBM were supported by the US National Science Foundation (AGS 1848724). EY's work has been partially supported by AFOSR (FA9550-20-1-0119) and NSF (AGS-1848730 and AGS-2430006) as well as NASA-80NSSC23M0193. The Jicamarca Radio Observatory is a facility of the Instituto Geofísico del Perú operated with support from the NSF AGS-2213849 through Cornell University. MP's work has been partly supported by the Space-It Up project of the Italian Space Agency, ASI, and the Ministry of University and Research, MUR, under contract n.2024-5-E.O-CUP n. I53D24000060005. DO acknowledges the Development in Africa with Radio Astronomy (DARA) program for providing support during this research.

References

Alken, P. (2009). A quiet time empirical model of equatorial vertical plasma drift in the Peruvian sector based on 150 km echoes. *Journal of Geophysical Research*, *114*(A2), A02308. https://doi.org/10.1029/2008JA013751

Anderson, D., Anghel, A., Chau, J., & Veliz, O. (2004). Daytime vertical E× B drift velocities inferred from ground-based magnetometer observations at low latitudes. *Space Weather*, *2*(11), S11001. https://doi.org/10.1029/2004SW000095

Anderson, D., Anghel, A., Yumoto, K., Ishitsuka, M., & Kudeki, E. (2002). Estimating daytime vertical E×B drift velocities in the equatorial F-region using ground-based magnetometer observations. *Geophysical Research Letters*, *29*(12), 1596. https://doi.org/10.1029/2001GL014562

Bilitza, D., Pezzopane, M., Truhlik, V., Altadill, D., Reinisch, B. W., & Pignalberi, A. (2022). The international reference ionosphere model: A review and description of an ionospheric benchmark. *Reviews of Geophysics*, *60*(4), e2022RG000792. https://doi.org/10.1029/2022RG000792

Boudouridis, A., & Zesta, E. (2007). Comparison of Fourier and wavelet techniques in the determination of geomagnetic field line resonances. *Journal of Geophysical Research*, *112*(A8), A08205. https://doi.org/10.1029/2006JA011922

Burden, F., & Winkler, D. (2008). Bayesian regularization of neural networks, In *Methods in Molecular Biology, Artificial Neural Networks. Methods in Molecular BiologyTM*, D. J. Livingstone (eds), (Vol. 458, pp. 25–44). https://doi.org/10.1007/978-1-60327-101-1_3

Camporeale, E. (2019). The challenge of machine learning in space weather: Nowcasting and forecasting. *Space Weather*, *17*(8), 1166–1207. https://doi.org/10.1029/2018sw002061

Cesaroni, C., Pezzopane, M., Zuccheretti, M., Pica, E., Spogli, L., Okoh, D., et al. (2025). Establishing the first ionospheric observatory in Kenya: Early results from the NORISK project. *Advances in Space Research*, *75*(6), 4698–4713. https://doi.org/10.1016/j.asr.2025.01.051

Chau, J. L., & Woodman, R. F. (2004). Daytime vertical and zonal velocities from 150-km echoes: Their relevance to F-region dynamics. *Geophysical Research Letters*, *31*(17), L17801. https://doi.org/10.1029/2004GL020800

Chou, M.-Y., Yue, J., Sassi, F., McDonald, S., Tate, J., Pedatella, N., et al. (2023). Modeling the day-to-day variability of midnight equatorial plasma bubbles with SAMI3/SD-WACCM-X. *Journal of Geophysical Research: Space Physics*, *128*(5), e2023JA031585. https://doi.org/10.1029/2023JA031585

Coley, W. R., & Heelis, R. A. (1989). Low-latitude zonal and vertical ion drifts seen by DE-2. *Journal of Geophysical Research*, *94*(A6), 6751–6761.

Dubazane, M. B., & Habarulema, J. B. (2018). An empirical model of vertical plasma drift over the African sector. *Space Weather*, *16*(6), 619–635. https://doi.org/10.1029/2018SW001820

Fang, T.-W., Akmaev, R. A., Stoneback, R. A., Fuller-Rowell, T., Wang, H., & Wu, F. (2016). Impact of midnight thermosphere dynamics on the equatorial ionospheric vertical drifts. *Journal of Geophysical Research: Space Physics*, *121*(5), 4858–4868. https://doi.org/10.1002/2015ja022282

Fejer, B. G., Farley, D. T., Woodman, R. F., & Calderon, C. (1979). Dependence of equatorial F region vertical drifts on season and solar cycle. *Journal of Geophysical Research*, *84*(A10), 5792–5796. https://doi.org/10.1029/ja084ia10p05792

Fejer, B. G., Jensen, J. W., & Su, S.-Y. (2008). Quiet time equatorial F region vertical plasma drift model derived from ROCSAT-1 observations. *Journal of Geophysical Research*, *113*(A5). https://doi.org/10.1029/2007JA012801

Harding, B. J., Serrano, M. C., Gasque, L. C., Joanne Wu, Y.-J., Maute, A., & Immel, T. J. (2025). Wind-driven variability in the prereversal enhancement of the equatorial vertical plasma drift: Climatologies observed by ICON. *Journal of Geophysical Research: Space Physics*, *130*(1), e2024JA033279. https://doi.org/10.1029/2024JA033279

Heelis, R. A., Depew, M. D., Chen, Y. J., & Perdue, M. D. (2022). Ionospheric connections (ICON) ion velocity meter (IVM) observations of the equatorial ionosphere at solar minimum. *Space Science Reviews*, *218*(62), 68. https://doi.org/10.1007/s11214-022-00936-w

Huang, C. M., Richmond, A. D., & Chen, M.-Q. (2005). Theoretical effects of geomagnetic activity on low-latitude electric fields. *Journal of Geophysical Research*, *110*, A05312. https://doi.org/10.1029/2004JA010994

Hysell, D. L., Kirchman, A., Harding, B. J., Heelis, R. A., & England, S. L. (2023). Forecasting equatorial ionospheric convective instability with ICON satellite measurements. *Space Weather*, *21*(5), e2023SW003427. https://doi.org/10.1029/2023sw003427

Hysell, D. L., Kirchman, A., Harding, B. J., Heelis, R. A., England, S. L., Frey, H. U., & Mende, S. B. (2024). Using ICON satellite data to forecast equatorial ionospheric instability throughout 2022. *Space Weather*, *22*(3), e2023SW003817. https://doi.org/10.1029/2023sw003817

Immel, T. J., England, S. L., Harding, B. J., Wu, Y. J., Maute, A., Cullens, C., et al. (2023). The ionospheric connection explorer—Prime mission review. *Space Science Reviews*, *219*(5), 41. https://doi.org/10.1007/s11214-023-00975-x

Kudeki, E., Bhattacharyya, S., & Woodman, R. F. (1999). A new approach in incoherent scatter F region E×B drift measurements at Jicamarca. *Journal of Geophysical Research*, *104*(A12), 28145–28162. https://doi.org/10.1029/1998JA900110

MacKay, D. J. C. (1992). A practical Bayesian framework for backpropagation networks. *Neural Computation*, *4*(3), 415–447. https://doi.org/10.1162/neco.1992.4.3.448

Poole, A. W. V., & McKinnell, L.-A. (2000). On the predictability of foF2 using neural networks. *Radio Science*, *35*(1), 225–234. https://doi.org/10.1029/1999RS900105

Richmond, A. D. (1973). Equatorial electrojet-I. Development of a model including winds and instabilities. *Journal of Atmospheric and Terrestrial Physics*, *35*(6), 1082–1103. https://doi.org/10.1016/0021-9169(73)90007-X

Scarselli, F., & Tsoi, A. C. (1998). Universal approximation using feedforward neural networks: A survey of some existing methods, and some new results. *Neural Networks*, *11*(1), 15–37. https://doi.org/10.1016/s0893-6080(97)00097-x

Scherliess, L., & Fejer, B. G. (1999). Radar and satellite global equatorial F region vertical drift model. *Journal of Geophysical Research*, *104*(A4), 6829–6842. https://doi.org/10.1029/1999ja900025

Shidler, S. A., & Rodrigues, F. S. (2020). Modeling equatorial ionospheric vertical plasma drifts using machine learning. *Earth Planets Space. 2020*, *72*(1), 102. https://doi.org/10.1186/s40623-020-01227-w

Stoneback, R., Heelis, R., Burrell, A., College, A., Fejer, B. G., & Pacheco, E. (2011). Observations of quiet time vertical ion drift in the equatorial ionosphere during the solar minimum period of 2009. *Journal of Geophysical Research*, *116*(A12), A12327. https://doi.org/10.1029/2011JA016712

Valladares, C. E., & Chau, J. L. (2012). The low-latitude ionosphere sensor network: Initial results. *Radio Science*, *47*(4), RS0L17. https://doi.org/10.1029/2011RS004978

Yizengaw, E., & Groves, K. M. (2018). Longitudinal and seasonal variability of equatorial ionospheric irregularities and electrodynamics. *Space Weather*, *16*(8), 948–968. https://doi.org/10.1029/2018SW001980

Yizengaw, E., & Moldwin, M. B. (2009). African Meridian B-field education and research (AMBER) array. *Earth, Moon, and Planets*, *104*(1–4), 237–246. https://doi.org/10.1007/s11038-008-9287-2

Yizengaw, E., Moldwin, M. B., Mebrahtu, A., Damtie, B., Zesta, E., Valladares, C. E., & Doherty, P. H. (2011). Comparison of storm time equatorial ionospheric electrodynamics in the African and American sectors. *Journal of Atmospheric and Solar-Terrestrial Physics*, *73*(1), 156–163. https://doi.org/10.1016/j.jastp.2010.08.008

Yizengaw, E., Moldwin, M. B., Zesta, E., Biouele, C. M., Damtie, B., Mebrahtu, A., et al. (2014). The longitudinal variability of equatorial electrojet and vertical drift velocity in the African and American sectors. *Annals of Geophysics*, *32*(3), 231–238. https://doi.org/10.5194/angeo-32-231-2014

Zhang, R., Liu, L., Chen, Y., & Le, H. (2024). The day-to-day variability of the dayside equatorial ionospheric plasma drifts and neutral winds observed by ICON. *Geophysical Research Letters*, *51*(8), 948–968. https://doi.org/10.1029/2024GL108980